DOI:
10.1002/nbm.4087

Document Version
Publisher's PDF, also known as Version of record

Received: 20 April 2018 | Revised: 12 February 2019 | Accepted: 14 February 2019

DOI: 10.1002/nbm.4087

RESEARCH ARTICLE

WILEY NMR IN BIOMEDICINE

Magnetic resonance elastography of skeletal muscle deep tissue injury

Jules L. Nelissen[1,2,3] | Ralph Sinkus[4] | Klaas Nicolay[1] | Aart J. Nederveen[3] | Cees W.J. Oomens[5] | Gustav J. Strijkers[2]

[1] Biomedical NMR, Biomedical Engineering, Eindhoven University of Technology, Eindhoven, The Netherlands

[2] Biomedical Engineering and Physics, Academic Medical Center, Amsterdam, The Netherlands

[3] Department of Radiology and Nuclear Medicine, Academic Medical Center, Amsterdam, The Netherlands

[4] Image Sciences & Biomedical Engineering, King's College London, London, UK

[5] Soft Tissue Engineering and Mechanobiology, Biomedical Engineering, Eindhoven University of Technology, The Netherlands

Correspondence
Jules L. Nelissen, Department of Radiology and Nuclear Medicine, Room B1-223, Academic Medical Center, Meibergdreef 9, 1105 AZ Amsterdam, The Netherlands.
Email: j.l.nelissen@gmail.com

Funding information
Dutch Technology Foundation (STW), Grant/Award Number: 12398; Myo-MRI COST action, Grant/Award Number: BM1304-250716-080500

The current state-of-the-art diagnosis method for deep tissue injury in muscle, a subcategory of pressure ulcers, is palpation. It is recognized that deep tissue injury is frequently preceded by altered biomechanical properties. A quantitative understanding of the changes in biomechanical properties preceding and during deep tissue injury development is therefore highly desired. In this paper we quantified the spatial–temporal changes in mechanical properties upon damage development and recovery in a rat model of deep tissue injury.

Deep tissue injury was induced in nine rats by two hours of sustained deformation of the tibialis anterior muscle. Magnetic resonance elastography (MRE), T_2-weighted, and T_2-mapping measurements were performed before, directly after indentation, and at several timepoints during a 14-day follow-up.

The results revealed a local hotspot of elevated shear modulus (from 3.30 ± 0.14 kPa before to 4.22 ± 0.90 kPa after) near the center of deformation at Day 0, whereas the T_2 was elevated in a larger area. During recovery there was a clear difference in the time course of the shear modulus and T_2. Whereas T_2 showed a gradual normalization towards baseline, the shear modulus dropped below baseline from Day 3 up to Day 10 (from 3.29 ± 0.07 kPa before to 2.68 ± 0.23 kPa at Day 10, $P < 0.001$), followed by a normalization at Day 14.

In conclusion, we found an initial increase in shear modulus directly after two hours of damage-inducing deformation, which was followed by decreased shear modulus from Day 3 up to Day 10, and subsequent normalization. The lower shear modulus originates from the moderate to severe degeneration of the muscle. MRE stiffness values were affected in a smaller area as compared with T_2. Since T_2 elevation is related to edema, distributing along the muscle fibers proximally and distally from the injury, we suggest that MRE is more specific than T_2 for localization of the actual damaged area.

Abbreviations used: EPUAP, European Pressure Ulcer Advisory Panel; FEA, finite element analysis; MDX, muscular dystrophin X-linked-deficient; NPUAP, National Pressure Ulcer Advisory Panel; ROI, region-of-interest; TA, tibialis anterior

KEYWORDS

biomechanical properties, deep tissue injury, magnetic resonance elastography, MRI, muscle damage, pressure wound, skeletal pressure ulcer

1 | INTRODUCTION

Sustained deformation of skeletal muscle in the proximity of bony structures may lead to deep tissue injury, which is one of the subcategories in the pressure ulcer classification system by the National and European Pressure Ulcer Advisory Panel (NPUAP/EPUAP).[1-5] Deep tissue injury commonly starts at the bone-skeletal muscle interface, and therefore is initially invisible and could remain undetected for days or weeks. As soon as the injury becomes visible as a purple or maroon discolored skin spot at the skin surface, it might progress rapidly into a severe and difficult to heal stage III or stage IV pressure ulcer.[5,6] Intensive- and acute-care patients, hospice patients, as well as people that require long-term care, for example, after a spinal cord injury or stroke, are at particular high risk of developing a deep tissue injury.[7] Deep tissue injury is related to increased morbidity and mortality and puts a significant cost burden on the healthcare system.[6,8-13]

Palpation is one of the oldest ways by which medical doctors perform a physical examination to detect disease. Also, for the detection of pressure ulcers, experienced clinicians and wound nurses frequently use palpation.[14,15] In fact, in the international pressure ulcer guidelines, palpation is included as one of the diagnostic tools. In the section describing deep tissue injury it reads: "The area may be preceded by tissue that is painful, firm, mushy, boggy, warmer or cooler as compared to adjacent tissue".[16] However, the description is of a rather qualitative nature. A quantitative understanding of the changes in tissue biomechanical properties preceding and during wound development is therefore highly desired.

Most of the current knowledge on changes in biomechanical properties related to deep tissue injury and pressure ulcers in general were obtained from controlled indentation experiments in animals and finite element analysis (FEA).[17-27] One of the well-established animal models of deep tissue injury involves the deformation of the rat tibialis anterior (TA) muscle with a custom loading device that can be placed in a MRI scanner for imaging during the development of the damage.[19,27] Several MRI and histopathologic readouts were employed to provide a comprehensive understanding of the damage development, recovery, and regeneration in this model.[18,21,25,28,29] It was found that the initial tissue response to deformation started at some distance from the center of indentation, affecting a relatively large area. Secondly, a single indentation of the TA muscle resulted in muscle damage that required at least two weeks to recover. Finally, MRI provided specific imaging parameters with diagnostic relevance for deep tissue injury-related muscle damage development and remodeling. T_2 and T_2-weighted MRI corresponded with edema, increased interstitial space, muscle cell damage, inflammatory onset, and inflammation. T_2^* provided a readout of tissue perfusion, hemorrhages, and inflammation. Diffusion-weighted imaging is sensitive to the integrity of the tissue microstructure and reflects muscle degeneration and edema, as well as extracellular matrix remodeling during the muscle remodeling processes. Time of flight MR angiography provided information on occlusion of blood flow during the indentation period.[29] Furthermore, the use of an animal-specific FEA model, for which the geometry and loading conditions were derived from MRI, supplied estimations of the local tissue deformations.[30] This combined experimental-numerical approach resulted in new understandings of the biomechanical conditions that contribute to the development of deep tissue injury.[26] In those previous studies, the involved tissues were always considered to have homogeneous material properties (stiffness). Because the entire experiment was kinematically driven, with a described displacement of the indenter and a fixation of the leg of the animal, the local tissue deformations could be determined without accurate knowledge of the material properties. For the studies in the current paper it is hypothesized that, due to changes in the tissue as a result of the mechanical load, local changes in stiffness will occur leading to heterogeneous material properties. This requires a new method to determine these local properties..[6,31-35]

The aim of this study was therefore to quantify the spatial–temporal changes in skeletal muscle mechanical properties upon damage development and (partial) recovery in the rat model of deep tissue injury. For this purpose, we employed the recently introduced rat magnetic resonance elastography (MRE) setup, which facilitates direct quantification of muscle shear modulus values.[27] This setup enables MRE estimations of local muscle tissue mechanical properties pre, during (not shown), and post-indentation of the rat TA muscle in the MRI scanner.

2 | METHODS

2.1 | Animal model

A total of nine Sprague–Dawley rats (♀, 11-week-old, Charles River, Paris, France) were included. Animals were housed under standard laboratory conditions with a 12-h light/dark cycle and were maintained on a standard diet and with access to water ad libitum. All animal experiments were approved by the Animal Care and Use Committee of Maastricht University (protocol 2013–047, Maastricht University, Maastricht, The Netherlands) and performed in accordance with Directive 2010/63/EU for animal experiments in the European Union.

Figure 1 shows the timeline of the longitudinal study. MRE, T_2-weighted, and T_2-mapping measurements were performed pre and post-2 h damage-inducing deformation of the TA muscle at Day 0, as well as at Day 3, 5, 7, 10, and 14. The T_2-weighted and T_2-mapping measurements

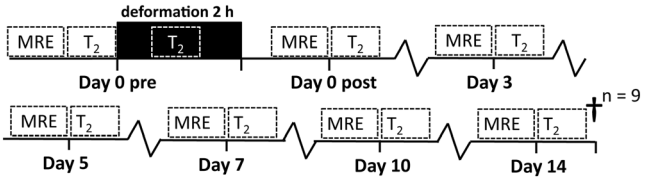

FIGURE 1 Timeline of the longitudinal study. Magnetic resonance Elastography measurements are indicated by MRE in the timeline, and T_2-weighted and T_2-mapping measurements are indicated by T_2 in the timeline. All animals were measured pre, during, and post-2 h of deformation at day 0, and at day 3, 5, 7, 10, and 14. After the last measurement at day 14, all animals were sacrificed (indicated by †)

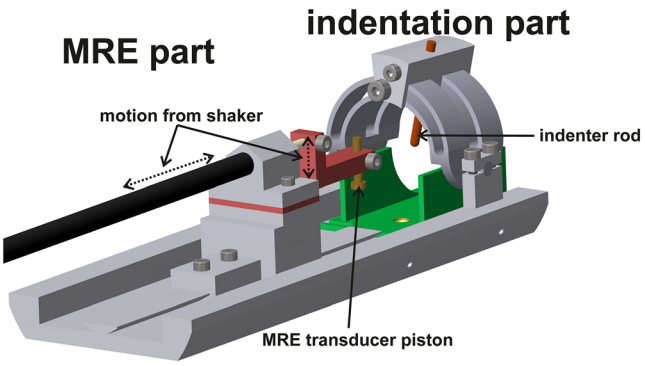

FIGURE 2 Schematic of MR-compatible setup consisting of an indentation and MRE part. Indenter rod and MRE transducer piston are indicated with a label. The MRE transducer piston is brought into motion via a drive rod attached to an electromagnetically driven shaker and cantilever

were also performed during the period of deformation. The rat was placed in supine position in the MR compatible indentation and MRE setup and anesthetized with isoflurane (4.0 vol.% for induction, 1.0–2.0 vol.% for maintenance) in 0.6 L/min medical air.[27] To review briefly, the setup consisted of an indentation and MRE part (Figure 2). The indenter rod was positioned on the rat's TA muscle using a movable indenter holder and rotatable half arch. The MRE transducer piston is brought into motion via a drive rod attached to an electromagnetically driven shaker (LDS V201, Brüel and Kjaer, Royston, UK) and cantilever. Buprenorphine (0.05 mg/kg subcutaneously) was administered for analgesia. Eye ointment was applied to prevent eye dehydration. Body temperature was maintained at 35–37°C with a heating blanket and monitored with a rectal temperature sensor. Respiration was monitored with a balloon pressure sensor placed on the abdomen and kept stable by adjusting the anesthesia. The right leg of the rat was shaved and positioned in an u-shaped profile filled with alginate molding substance for firm fixation and susceptibility matching. The TA muscle in the rat hindleg was deformed by manually pushing the indenter rod into the muscle. The extent and severity of damage caused by deformation of the TA and the time course of recovery is variable among rats and depends on various factors, including the individual rat leg anatomy, the depth and angle of indentation, the induced strain in the muscle as well as the extent of ischemia. The duration of 2 h deformation was in line with previous studies, in which different durations of deformation, ischemia and reperfusion were studied.[30] During the deformation period, part of the alginate was removed to make the TA muscle assessable for the indenter. The MRE transducer piston was coupled to the alginate, close to the tendon at the distal side of the TA muscle. After the last measurement at Day 14, the rats were sacrificed by means of exsanguination from the inferior vena cava. This procedure was performed under anesthesia and after administration of analgesia.

2.2 | MRI

Measurements were performed with a 7.0 T small animal MRI scanner (Bruker BioSpin MRI GmbH, Ettlingen, Germany) equipped with a 660 mT/m, 4570 T/m/s gradient coil (BGA-12S HP, Bruker BioSpin MRI GmbH). An 86-mm-inner-diameter quadrature transmit coil was used in combination with a 20 or 30 mm receive surface coil, placed on top of the TA muscle inside the indentation device.

For anatomical information, axial T_2-weighted MRI was performed with a 2D rapid imaging with refocused echoes (RARE) sequence. The TA muscle was imaged by 16 1-mm-thick slices with field of view (FOV) = 40 x 40 mm^2, a 512 x 512 reconstruction matrix (MTX), number of averages (NEX) = 5, RARE factor = 8, effective echo time (TE_{eff}) = 40 ms, repetition time (TR) = 2500 ms, chemical-shift selective (CHESS) fat suppression, and acquisition time 13 min.

MRE images were acquired with an in-house-developed spin echo echo-planar-imaging (SE-EPI) MRE sequence with CHESS fat suppression in coronal orientation. Motion encoding gradients (MEG) were placed symmetrically around the SE inversion RF pulse. The other parameters were: number of slices = 18, slice thickness = 0.3125 mm, FOV = 30 x 60 mm^2, MTX = 96 x 192, TE = 26.2 ms, TR = 1000 ms, actuator and MEG

frequency = 900 Hz, MEG-shape = sinusoidal, number of MEG cycles = 5, MEG amplitude = 660 mT/m, number of EPI segments = 4, NEX = 8, number of MRE phase offsets = 8, number of encoding directions = 3 (slice, phase, frequency encoding) plus 1 reference, and acquisition time ~16 min.

For indication of the location of skeletal muscle damage, T_2-mapping MRI was performed with a 2D multi-slice multi-echo (MSME) sequence in coronal orientation. The other acquisition parameters were: CHESS fat suppression, number of slices = 6, slice thickness = 0.9375 mm, FOV = 60 x 30 mm^2, MTX = 512 x 256, 33% zero filling, 20 echoes (TE = 10.18–203.5 ms), TR = 3200 ms, and acquisition time ~10 min, covering the same imaging volume as the MRE acquisition.

2.3 | Data analysis

The MRE acquisitions provide phase data for the harmonic vibrations which are proportional to the harmonic displacements. The displacement data can be converted to maps of viscoelastic properties with a local inversion algorithm, ie images representing the local tissue linear elastic dynamic shear modulus G_d, loss shear modulus G_l, magnitude of the complex shear modulus $\left|G^*\right| = \sqrt{{G_d}^2 + {G_l}^2}$, and phase angle $\phi = \mathrm{atan}\left(\frac{G_l}{G_d}\right)$. The inversion process assumes linear (visco) elasticity, isotropy, and local homogeneity for all tissues, and aims to solve the partial differential equation: $-\rho\omega^2\mathbf{q}(x) = G^*\nabla^2\mathbf{q}(x)$, where G^* is the complex shear modulus, ρ is the density, $\mathbf{q}$ is the curl of the complex displacement vector ($\boldsymbol{q}(x) = \nabla \times u(x)$) derived from the MRE phase data, and ω is the known angular frequency.

Full details of the inversion algorithm implemented in the ROOT data analysis framework (ROOT 5.34/17, CERN, Meyrin, Switzerland) were previously described by Sinkus et al.[36-38] To review briefly, the slice, phase, frequency and reference encoded MRE phase images were unwrapped and filtered using a three-dimensional Gaussian filter with 3 x 3 x 3 support and σ = 1 voxel. To remove the compressional wave component the curl was calculated on a stencil of 3 x 3 x 3 pixels, followed by reconstruction of the viscoelastic maps using the direct inversion method.[39]

Quantitative T_2-maps were obtained by pixel-wise fitting the MR signal to $S(TE) = S(0)e^{-TE/T_2}$ (Mathematica 10, Wolfram Research, Champaign, IL, USA). Pixels with $R^2 < 0.9$ were excluded from subsequent analysis.

After inversion of the acquired MRE data, a stack of three middle slices—matching one T_2-mapping slice—were averaged. The MRE-averaged stack was interpolated to match the T_2-mapping resolution. Masking of the background was applied to all images. Region-of-interest (ROI)-based analysis of this selected volume was performed (Matlab R2016a, The Mathworks, Inc., Natick, MA, USA). The ROI was defined by manually outlining the whole TA muscle, and by selecting a circular ROI of 2 x the indenter's diameter around the center of indentation, on the first echo of the T_2-mapping dataset. Representative positioning of the circular ROI and whole TA ROI is shown in Figure 3E. Mean values of T_2, G_d, G_l,|G*| and φ were determined in both ROIs at all timepoints. A repeated measures analysis using a linear mixed model with Bonferroni correction was conducted on both ROIs to test for significant differences of all timepoints with respect to baseline (pre-deformation) (SPSS 23, IBM, Armonk, NY, USA). MRE shear moduli with a mean nonlinearity >50% in the ROI were excluded from statistical analysis. The nonlinearity is a measure of the quality of the delivered MRE shear wave in the tissue and is defined as the ratio of the amplitude of the second harmonic of the vibrational frequency to the base frequency.[40] Therefore, a perfect shear wave without any noise will lead to a nonlinearity of 0. Contrarily, if the second harmonic is as powerful as the base frequency, the ratio will be 1, ie 100%.

3 | RESULTS

Anatomical T_2-weighted MRI was used for planning of the coronal T_2-mapping and MRE imaging volume. Representative axial T_2-weighted MR images of a central slice acquired pre, during, and post-2 h of deformation are shown in Figure 3A, B and C, respectively. In Figure 3A, the TA muscle, tibia bone, and planned coronal imaging volume are indicated with arrows. The central coronal slice location used for all analysis is indicated with a dashed line. The indenter, filled with a liquid solution of $CuSO_4$, was clearly visible (indicated by an arrow in Figure 3B). Post-deformation, the whole TA compartment was hyperintense (Figure 3C). A movie looping over all acquired slices, from ankle to knee, of pre, during, and post-2 h of deformation, is included in the supporting information for this article (Supplemental I).

The corresponding coronal T_2-maps, MRE phase-image snapshots, and dynamic shear modulus G_d-maps of pre and post-deformation of the planned central coronal slice are shown in Figure 3D-I. The T_2-maps post-deformation showed a large region of elevated T_2 values in a muscle-fiber-like pattern, with somewhat lower values in the center of indentation compared with the immediate surroundings (Figure 3E, green arrow). The MRE phase-image snapshot post-deformation showed a distinct change in wave pattern compared with pre-deformation. A movie of all MRE phase-images of pre and post-2 h deformation can be found in the supporting information for this article (Supplemental II). A hotspot with increased shear dynamic shear modulus G_d values was observed near the center of indentation, which colocalized with the area of somewhat lower T_2 values (Figure 3E, green arrow).

T_2, G_d, G_l, and|G*|-maps during the full time course of damage induction and recovery of one representative animal with extensive damage of the TA muscle are shown in Figure 4. Maps at Day 0 pre were from healthy muscle to which all other timepoints were compared. Similar to the

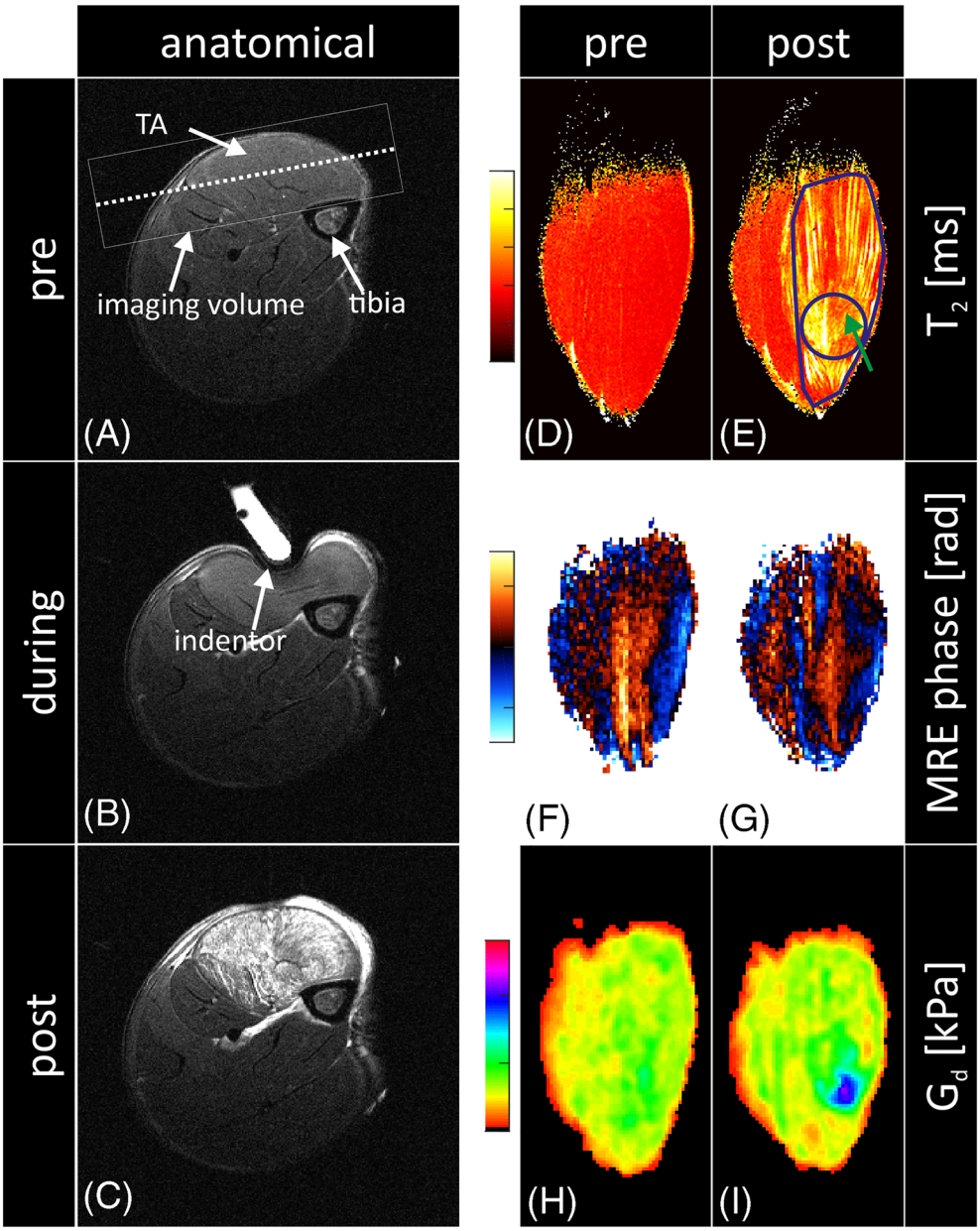

FIGURE 3 (A-C) axial anatomical images, (D,E) coronal T_2-maps, (F,G) MRE phase-image snapshots of a 900 Hz SE-EPI-MRE acquisition with eight phase offsets, and (H,I) dynamic shear modulus G_d maps of a representative rat (RAT-009 of Figures 5 and 7) pre, during (axial anatomical only), and post-2 h deformation. TA muscle, tibia bone, and planned coronal imaging volume with selected central slice (A, dashed line) are indicated by arrows in the anatomical image pre-deformation (A). Anatomical image during deformation shows the indentation of the TA muscle with the indenter (B, indicated by arrow). High signal intensity was observed in the TA muscle postdeformation (C). Coronal T_2-map postdeformation showed elevated T_2 values in a muscle-fiber-like pattern, with lower values near the indentation center (E, green arrow). The MRE phase snapshot images showed a distinct change in wave pattern between (F) pre and (G) post-deformation. Post-deformation, a hotspot of increased dynamic shear modulus G_d was found (I). Legends for the color scaling of the T_2 (0–100 ms), MRE phase snapshot ($-\pi$ to π rad), and G_d (0–14 kPa) are shown to the left of the panels. Representative selection of the circular and whole TA ROIs is illustrated with a blue line on the coronal T_2-map post-deformation (E)

example shown in Figure 3 at Day 0 after, indentation resulted in elevated T_2 values in the whole TA muscle body and a hotspot with locally increased shear modulus values and lower T_2 values. The local hotspot persisted up to five days after damage induction. From Day 7 onwards T_2 returned to baseline values whereas shear modulus values became regionally somewhat lower compared with baseline at the later timepoints.

Individual time courses of the mean T_2 and G_d values of the nine animals, determined in the circular ROI of 2 x the diameter of the indenter, are shown in Figure 5. A detailed summary of the mean shear modulus, phase angle, and T_2 values, including statistics, in the whole TA ROI and circular ROI at all timepoints, is given in Table 1. Distinctly different T_2 and G_d time courses were observed. Whereas T_2 initially increases with a peak at Day 3, followed by a gradual decrease over time towards baseline values, G_d showed a peak of elevated stiffness directly after end of deformation at Day 0, subsequently continued with a drop below baseline values from Day 3 up to Day 10, followed by normalization to baseline at

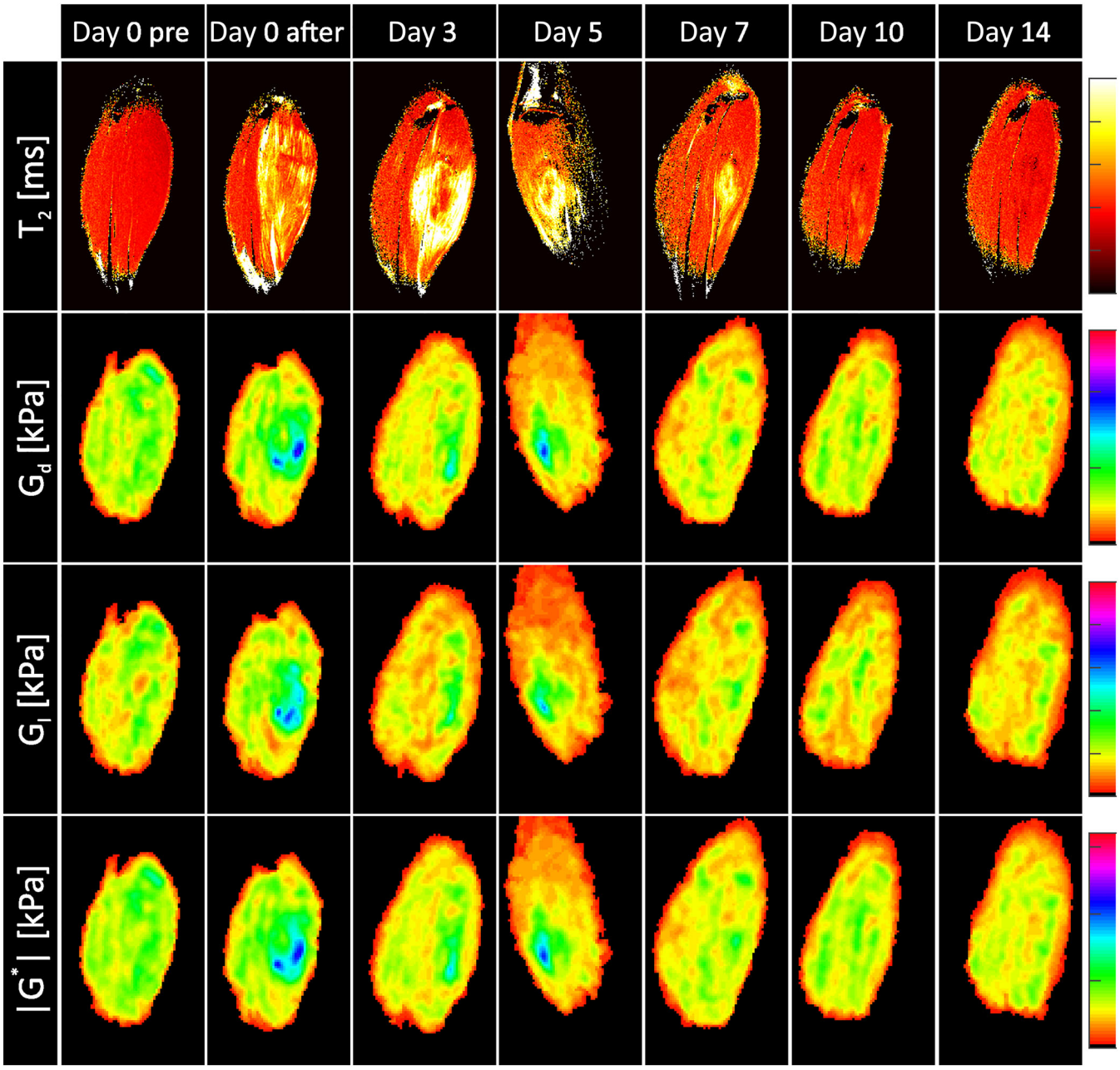

FIGURE 4 Longitudinal MRE and T_2-mapping readouts of one representative rat (RAT-001 of Figure 5). From top to bottom: Coronal T_2, G_d, G_l, and |G*|maps. Legends for the color scaling of the T_2 (0–100 ms), G_d (0–14 kPa), G_l (0–10 kPa), and |G*|(0–16 kPa) maps are shown on the right. The mean T_2 and G_d time courses of a circular ROI of 2 x the indenter's diameter of this rat (RAT-001) are also shown in Figure 5

Day 14. Interestingly, the phase angle φ remained constant over time. The time courses of all quantified MRE shear modulus parameters (G_d, G_l, and |G*|) and T_2 are included in the supporting information for this article (Supplemental III).

Figure 5 also illustrates that not all animals had the same response in time after indentation. As an example, we discuss two distinctly different cases, RAT-001 (Figure 5, green line) and RAT-002 (Figure 5, magenta line). The quantitative parameter maps of RAT-001 and RAT-002 are shown in Figures 4 and 6, respectively. In RAT-002, injury from indentation was relatively mild, with T_2, G_d, G_l, and |G*|values not significantly different from baseline. By contrast, indentation in RAT-001 resulted in extensive TA muscle damage.

A correlation plot of T_2 versus G_d for all animals at all timepoints is shown in Figure 7. Each timepoint is indicated with a different symbol. One rat with extensive damage of the TA muscle (RAT-009) is depicted with green symbols to highlight the T_2 and G_d values of this representative animal. Overall, there exists no linear relation between T_2 and G_d. Instead, the initial muscle damage is characterized by increased T_2 and G_d values (Figure 7, red arrow), whereas during recovery G_d decrease precedes T_2 normalization (Figure 7, green arrow). For most animals G_d was temporarily lower than baseline values during recovery.

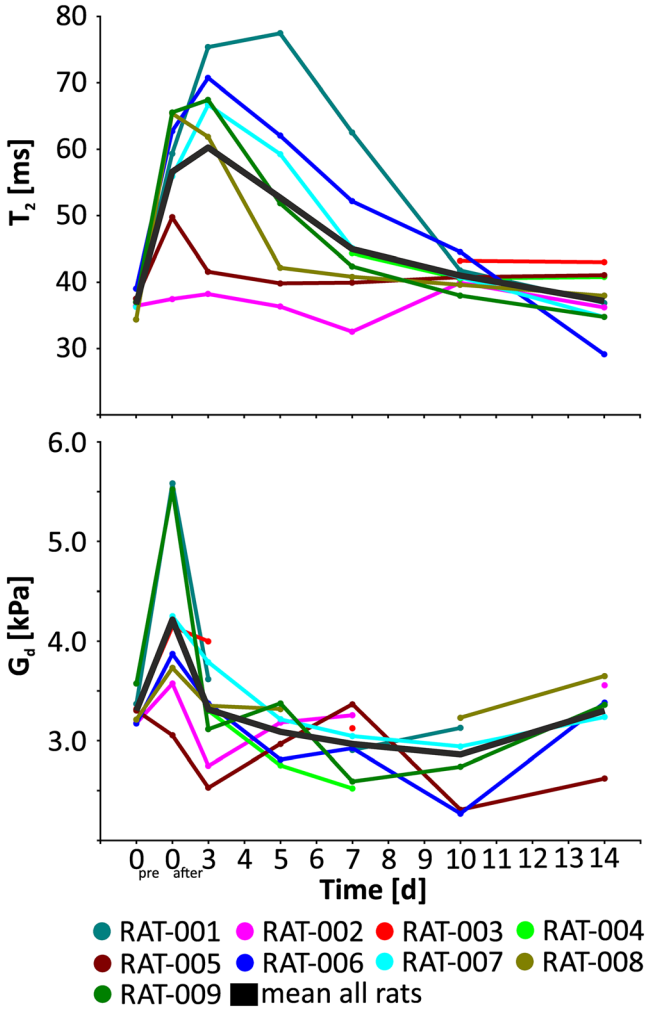

FIGURE 5 Mean T_2 and G_d values of the circular ROI of 2 x indenter's diameter of all individual animals over time. Each colored line results from a single rat. Data points on the line are the measurement timepoints. The mean of all the rats is depicted with the black line. The legend is depicted at the bottom of the figure. RAT-001 was depicted in Figure 4. RAT-009 was depicted in Figure 3. RAT-002 is depicted in Figure 6

TABLE 1 Quantitative MRE and T_2-mapping parameter values of whole TA ROI and indentation center ROI

	Day 0 pre	Day 0 after	Day 3	Day 5	Day 7	Day 10	Day 14
Whole TA							
T_2 [ms]	38 ± 1	55 ± 9*	50 ± 11*	44 ± 11	41 ± 5	41 ± 2*	38 ± 4
G_d [kPa]	3.29 ± 0.07	3.32 ± 0.32	2.97 ± 0.23*	3.01 ± 0.25	2.82 ± 0.23*	2.68 ± 0.23***	3.09 ± 0.24
G_l [kPa]	2.11 ± 0.06	2.24 ± 0.26	1.90 ± 0.14*	1.96 ± 0.17	1.83 ± 0.17*	1.70 ± 0.12***	1.97 ± 0.20
|G*| [kPa]	3.94 ± 0.08	4.04 ± 0.41	3.55 ± 0.27*	3.63 ± 0.30	3.39 ± 0.28*	3.20 ± 0.25**	3.69 ± 0.31
φ [rad]	0.57 ± 0.01	0.59 ± 0.02	0.57 ± 0.02	0.58 ± 0.01	0.58 ± 0.02	0.57 ± 0.03	0.56 ± 0.02
Indentation center							
T_2 [ms]	37 ± 1	57 ± 10*	60 ± 15**	53 ± 15*	45 ± 9	41 ± 2**	37 ± 4
G_d [kPa]	3.30 ± 0.14	4.22 ± 0.90	3.31 ± 0.47	3.09 ± 0.25	2.97 ± 0.30	2.86 ± 0.38	3.30 ± 0.36
G_l [kPa]	2.15 ± 0.08	2.90 ± 0.66	2.17 ± 0.27	1.98 ± 0.24	1.99 ± 0.27	1.84 ± 0.18	2.20 ± 0.40
|G*| [kPa]	3.97 ± 0.13	5.17 ± 1.13	4.00 ± 0.54	3.70 ± 0.33	3.60 ± 0.38	3.43 ± 0.41	4.01 ± 0.51
φ [rad]	0.58 ± 0.03	0.60 ± 0.03	0.58 ± 0.02	0.57 ± 0.03	0.59 ± 0.04	0.58 ± 0.03	0.58 ± 0.05

Mean ± SD T_2, G_d, G_l, |G*|, and φ values of whole TA ROI and indentation center (2 x indenter's diameter) ROI. The asterisk (*) indicates a significant difference (*** for $P < 0.001$, ** for $P < 0.01$, * for $P < 0.05$) versus baseline value at Day 0 pre.

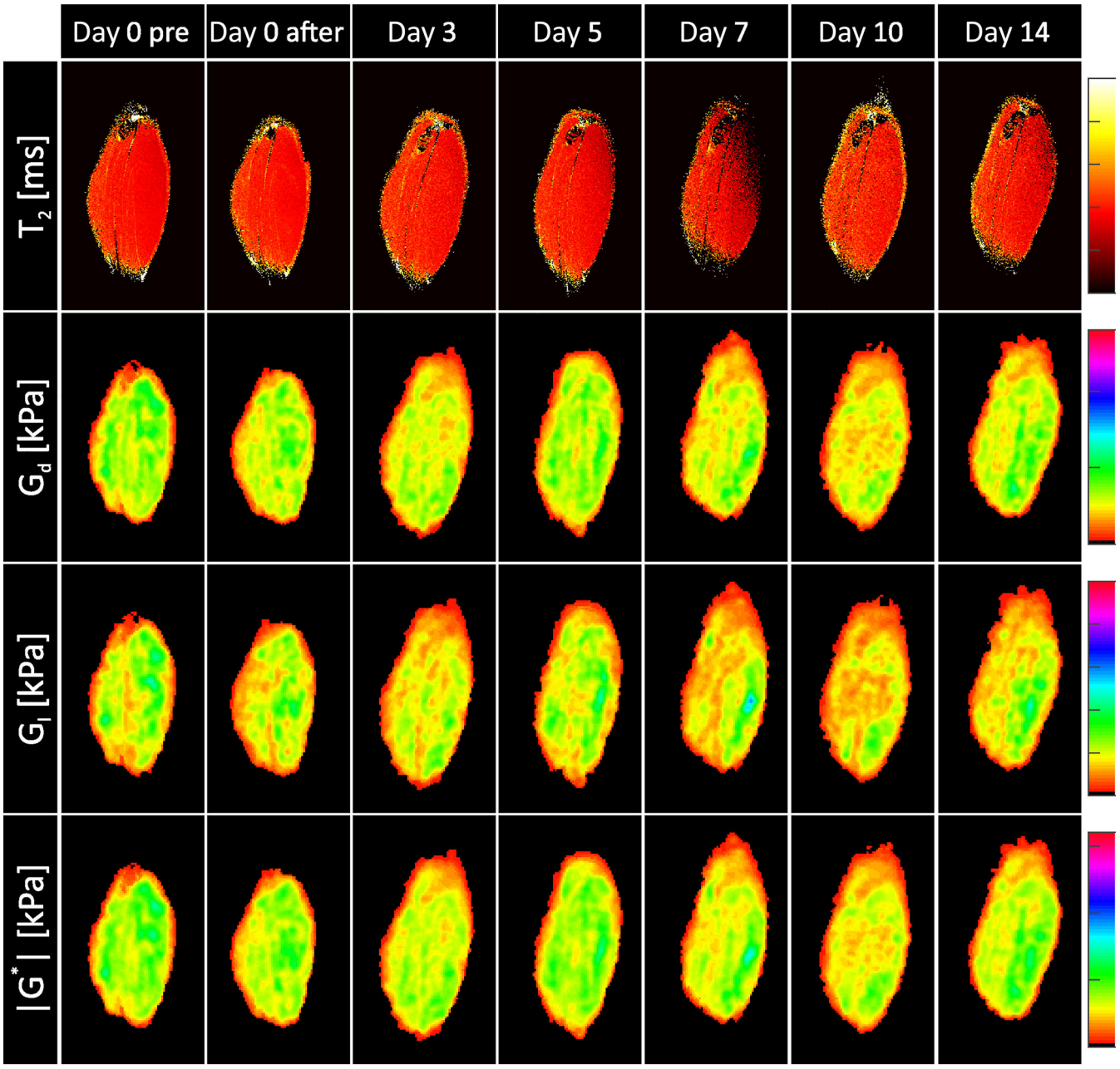

FIGURE 6 Longitudinal MRE and T_2-mapping readouts of one representative rat with mild to no damage of the TA muscle (RAT-002 of Figure 5). From top to bottom: Coronal T_2, G_d, G_l, and $|G^*|$maps. Legends for the color scaling of the T_2 (0–100 ms), G_d (0–14 kPa), G_l (0–10 kPa), and $|G^*|$(0–16 kPa) maps are shown on the right. The mean T_2 and G_d time course of a circular ROI of 2 x the indenter's diameter of this rat (RAT-002) was also shown in Figure 5

4 | DISCUSSION

The response of skeletal muscle deep tissue injury is known to follow a well-known pathway with multiple overlapping pathological processes.[29] Several studies have concluded that a single MRI contrast cannot capture all of the pathological processes involved in skeletal muscle damage,[22,25,28,41-53] which therefore warrants a multi-parametric approach using several complementary MRI readouts to characterize different aspects of injury and recovery. Furthermore, thus far there is limited knowledge on the spatio-temporal changes in the biomechanical properties of the muscle tissue following deformation-induced muscle damage. We therefore employed a multi-parametric approach, involving T_2-mapping for damage quantification and MRE for quantification of mechanical properties, to monitor changes in the muscle stiffness in relation to deformation-induced muscle damage.

MRE revealed a local hotspot of elevated G_d, G_l, and $|G^*|$near the center of deformation directly after load release at Day 0, whereas T_2 was elevated in a much larger area. This difference in spatial extend can be explained by higher specificity of T_2 for fluid accumulation, which diffuses

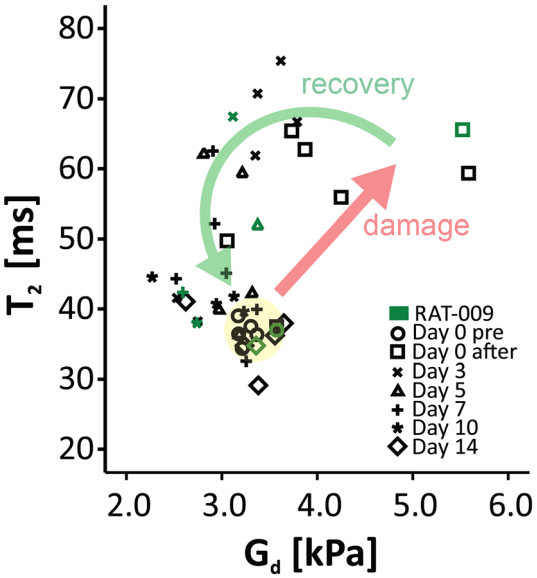

FIGURE 7 Correlation scatter plot between T_2 and G_d of all animals at all timepoints. The legend of the symbols used for the different timepoints is depicted in the bottom right corner. Green symbols refer to one representative rat (RAT-009) with extensive damage of the TA. The red and green arrows are guides to the eye and indicate the cycle of damage and recovery

proximally and distally along the muscle fibers after injury.[27] Similar to our results, Lv et al found elevated shear stiffness in skeletal muscle of rabbits up to 72 hours after crush injury with ultrasound elastography, which was attributed to swollen muscle cells and increased interstitial space.[54] During recovery there was a clear difference in the time course of the shear modulus and T_2. Whereas T_2 showed a gradual normalization towards baseline over a 14-day time span, G_d, G_l, and $|G^*|$shear moduli dropped below baseline from Day 3 up to Day 10, followed by normalization at Day 14. Decrease in shear stiffness values associated with diseased skeletal muscles, eg in myositis and hyperthyroid myopathy, was reported previously.[55,56] With the histopathological remodeling processes of deep tissue injury in mind, as previously reported by Nelissen et al, the lower shear modulus values likely originate from the moderate to severe degeneration of the TA muscle with massive necrosis, hemorrhage, edema, and inflammation.[29] The macroscopic MRE shear wave has shown to be highly sensitive to these changes in tissue microstructure based on the distribution and presence of microscopic scatterers.[57,58] However, the constant phase angle φ over time implies no change in the ratio of elastic to viscous properties of the TA muscle, whereas a reduction of the phase angle due to disorganization of the damaged muscle fibers was expected.[59] A possible explanation could be the precisely orchestrated process of skeletal muscle remodeling after damage, which is capable of preserving the muscle architectural organization.[60]

For the inversion of the MRE data, linear (visco) elastic isotropic material properties were assumed for skeletal muscle. Although this approach is used by several groups, it is a simplification for skeletal muscle which generally exhibits nonlinear viscoelastic anisotropic material behavior.[61,62] Others proposed the use of a linear (visco) elastic transverse isotropic material approach as an intermediate solution.[63-66] Using this approach, Qin et al found a decrease in anisotropic ratio, related to necrosis, in an MDX mouse model of diseased skeletal muscle.[67] However, to date the transverse isotropic MRE inversion is still rarely used, as muscle fiber directions obtained, for example by diffusion tensor imaging (DTI), are needed as input. Skeletal muscle DTI can be challenging in small animals and DTI measurements are lengthy.[68] Nevertheless, a combination of MRE and DTI acquisitions in one measurement would facilitate a transverse isotropic MRE inversion.[69] This might be achieved in a time-efficient manner by the use of advanced acquisition acceleration techniques for DTI and MRE such as multi-band imaging and compressed sensing.[70,71]

From the clinical perspective concerning prevention of (recurrence of) deep tissue injury, the observed lower stiffness during the recovery process of the wound has a very relevant and practical implication. It was shown by several groups that the critical strain threshold for the development of injury is reached at lower indentation force when muscle stiffness is lower.[31,72] This means that after initial injury the patient could be at higher risk of developing another deep tissue injury. Repeated muscle loading should therefore be avoided and preventive measures taken. In addition, the observed initial increase in shear stiffness direct after damage induction might be used for early diagnosis of deep tissue injury.

To conclude, in a rat model of deep tissue injury, a single 2 h-indentation of the TA muscle caused extensive damage, which required at least 14 days to recover. We measured an initial increase in muscle shear modulus values directly after the end of a period of damage-inducing deformation, which was followed by decreased shear modulus values from Day 3 up to Day 10, and subsequent normalization. MRE stiffness values were affected in a smaller area compared with T_2, suggesting that MRE might be more specific as T_2 for identification of the actual damaged area. Reloading of the affected muscle should be avoided at all times in order to allow recovery and decrease the risk of new injury.

ACKNOWLEDGEMENTS

The authors thank Tom Bruijnen, Martijn Blatter, Tom Schreurs and Larry de Graaf for help with the MRE sequence design and experimental setup, and Leonie Niesen, Jo Habets, Marije Janssen, Roy Lucassen, Carlijn Tijsen van Helvert, and David Veraart for biotechnical assistance. Invaluable advice on experimental design and methods by Willeke Traa and Jurgen Runge is gratefully acknowledged.

FUNDING INFORMATION

Dutch Technology Foundation (STW) project number 12398 (PI: Prof. Cees Oomens), and Myo-MRI COST action (BM1304-250716-080500).

ORCID

Jules L. Nelissen https://orcid.org/0000-0001-8840-6723
Ralph Sinkus https://orcid.org/0000-0002-6093-1654

Klaas Nicolay https://orcid.org/0000-0002-4179-616X

Aart J. Nederveen https://orcid.org/0000-0002-5477-973X

Cees W.J. Oomens https://orcid.org/0000-0002-3325-132X

Gustav J. Strijkers https://orcid.org/0000-0001-6700-5058

REFERENCES

1. Bouten CV, Oomens CWJ, Baaijens FP, Bader DL. The etiology of pressure ulcers: skin deep or muscle bound? *Arch Phys Med Rehabil*. 2003;84(4):616-619. https://doi.org/10.1053/apmr.2003.50038
2. Stekelenburg A, Gawlitta D, Bader DL, Oomens CW. Deep tissue injury: how deep is our understanding? *Arch Phys Med Rehabil*. 2008;89(7):1410-1413. https://doi.org/10.1016/j.apmr.2008.01.012
3. Black J. National Pressure Ulcer Advisory Panel's updated pressure ulcer staging system. *Adv Skin Wound Care*. 2007;20(5):269-274.
4. Beeckman D, Schoonhoven L, Fletcher J, et al. EPUAP classification system for pressure ulcers: European reliability study. *J Adv Nurs*. 2007;60(6):682-691. https://doi.org/10.1111/j.1365-2648.2007.04474.x
5. Ankrom MA, Bennett RG, Sprigle S, et al. Pressure-related deep tissue injury under intact skin and the current pressure ulcer staging systems. *Adv Skin Wound Care*. 2005;18(1):35-42.
6. Gefen A, Farid KJ, Shaywitz I. A review of deep tissue injury development, detection, and prevention: shear savvy. *Ostomy Wound Manage*. 2013;59(2):26-35.
7. Fleck CA. Suspected deep tissue injury. *Adv Skin Wound Care*. 2007;20(7):413-415. https://doi.org/10.1097/01.ASW.0000280206.96378.5b
8. Fleck CA. Deep tissue injury: what, why and when? *Wound Care Canada*. 2007;5(2):10-13.
9. Richbourg L, Smith J, Dunzweiler S. Suspected deep tissue injury evaluated by North Carolina WOC nurses. *J Wound Ostomy Cont Nurs*. 2011;38(6):655-660. https://doi.org/10.1097/WON.0b013e31823429e7
10. Brown G. Long-term outcomes of full-thickness pressure ulcers: healing and mortality. *Ostomy Wound Manage*. 2003;49(10):42-50.
11. Bennett G, Dealey C, Posnett J. The cost of pressure ulcers in the UK. *Age Ageing*. 2004;33(3):230-235. https://doi.org/10.1093/ageing/afh086
12. Dealey C, Posnett J, Walker A. The cost of pressure ulcers in the United Kingdom. *J Wound Care*. 2012;21(6):261-266. https://doi.org/10.12968/jowc.2012.21.6.261
13. Severens. The cost of illness of pressure ulcers in the Netherlands. *Adv Skin Wound Care*. 2002;15(2):72-77.
14. Black J, Baharestani M, Black S, et al. An overview of tissue types in pressure ulcers: a consensus panel recommendation. *Ostomy Wound Manage*. 2010;56(4):28-44.
15. Black JM, Brindle CT, Honaker JS. Differential diagnosis of suspected deep tissue injury. *Int Wound J*. 2016;13(4):531-539. https://doi.org/10.1111/iwj.12471
16. NPUAP/EPUAP/PPPIA. *Prevention and Treatment of Pressure Ulcers: Clinical Practice Guideline*. Perth, Australia: Cambridge Media; 2014.
17. Bosboom EMH, Bouten CVC, Oomens CWJ, Van Straaten HWM, Baaijens FPT, Kuipers H. Quantification and localisation of damage in rat muscles after controlled loading - a new approach to study the aetiology of pressure sores. *Med Eng Phys*. 2001;23(3):195-200. https://doi.org/10.1016/S1350-4533(01)00034-0
18. Bosboom EMH, Bouten CVC, Oomens CWJ, Baaijens FPT, Nicolay K. Quantifying pressure sore-related muscle damage using high-resolution MRI. *J Appl Physiol*. 2003;95(6):2235-2240. https://doi.org/10.1152/japplphysiol.01023.2001
19. Stekelenburg A, Oomens CWJ, Strijkers GJ, de Graaf L, Bader DL, Nicolay K. A new MR-compatible loading device to study in vivo muscle damage development in rats due to compressive loading. *Med Eng Phys*. 2006;28(4):331-338. https://doi.org/10.1016/j.medengphy.2005.07.005
20. Stekelenburg A. Compression-induced deep tissue injury examined with magnetic resonance imaging and histology. *J Appl Physiol*. 2006;100(6):1946-1954. https://doi.org/10.1152/japplphysiol.00889.2005

21. Loerakker S, Stekelenburg A, Strijkers GJ, et al. Temporal effects of mechanical loading on deformation-induced damage in skeletal muscle tissue. *Ann Biomed Eng*. 2010;38(8):2577-2587. https://doi.org/10.1007/s10439-010-0002-x
22. Stekelenburg A, Strijkers GJ, Parusel H, Bader DL, Nicolay K, Oomens CW. Role of ischemia and deformation in the onset of compression-induced deep tissue injury: MRI-based studies in a rat model. *J Appl Physiol*. 2007;102(5):2002-2011. https://doi.org/10.1152/japplphysiol.01115.2006
23. Ceelen KK, Stekelenburg A, Loerakker S, et al. Compression-induced damage and internal tissue strains are related. *J Biomech*. 2008;41(16):3399-3404. https://doi.org/10.1016/j.jbiomech.2008.09.016
24. van Nierop BJ, Stekelenburg A, Loerakker S, et al. Diffusion of water in skeletal muscle tissue is not influenced by compression in a rat model of deep tissue injury. *J Biomech*. 2010;43(3):570-575. https://doi.org/10.1016/j.jbiomech.2009.07.043
25. Loerakker S, Manders E, Strijkers GJ, et al. The effects of deformation, ischemia, and reperfusion on the development of muscle damage during prolonged loading. *J Appl Physiol*. 2011;111(4):1168-1177. https://doi.org/10.1152/japplphysiol.00389.2011
26. Coleman S, Nixon J, Keen J, et al. A new pressure ulcer conceptual framework. *J Adv Nurs*. 2014;70(10):2222-2234. https://doi.org/10.1111/jan.12405
27. Nelissen JL, de Graaf L, Traa WA, et al. A MRI-compatible combined mechanical loading and MR Elastography setup to study deformation-induced skeletal muscle damage in rats. *PLoS ONE*. 2017;12(1):e0169864. https://doi.org/10.1371/journal.pone.0169864
28. Loerakker S, Oomens CWJ, Manders E, et al. Ischemia-reperfusion injury in rat skeletal muscle assessed with T2-weighted and dynamic contrast-enhanced MRI. *Magn Reson Med*. 2011;66(2):528-537. https://doi.org/10.1002/mrm.22801
29. Nelissen JL, Traa WA, de Boer HH, et al. An advanced magnetic resonance imaging perspective on the etiology of deep tissue injury. *J Appl Physiol*. March 2018;124(6):1580-1596. https://doi.org/10.1152/japplphysiol.00891.2017
30. Oomens CWJ, Bader DL, Loerakker S, Baaijens FP. Pressure induced deep tissue injury explained. *Ann Biomed Eng*. 2015;43(2):297-305. https://doi.org/10.1007/s10439-014-1202-6
31. Loerakker S, Solis LR, Bader DL, Baaijens FPT, Mushahwar VK, Oomens CWJ. How does muscle stiffness affect the internal deformations within the soft tissue layers of the buttocks under constant loading? *Comput Methods Biomech Biomed Engin*. March 2013;2012:37-41. https://doi.org/10.1080/10255842.2011.627682
32. Gehin. Which techniques to improve the early detection and prevention of pressure ulcers? *Proc IEEE*. 2006;28:6057-6060.
33. Deprez J-F, Brusseau E, Fromageau J, Cloutier G, Basset O. On the potential of ultrasound elastography for pressure ulcer early detection. *Med Phys*. 2011;38(4):1943-1950. https://doi.org/10.1118/1.3560421
34. Gefen A, Gefen N, Linder-Ganz E, Margulies SS. In vivo muscle stiffening under bone compression promotes deep pressure sores. *J Biomech Eng*. 2005;127(3):512. https://doi.org/10.1115/1.1894386
35. Loerakker S. *The relative contributions of muscle deformation and Ischaemia to pressure ulcer development*. Eindhoven, the Netherlands: Universiteitsdrukkerij TU Eindhoven; 2011 https://doi.org/10.6100/IR716284.
36. Sinkus R, Lorenzen J, Schrader D, Lorenzen M, Dargatz M, Holz D. High-resolution tensor MR elastography for breast tumour detection. *Phys Med Biol*. 2000;45(6):1649-1664.
37. Sinkus R, Tanter M, Xydeas T, Catheline S, Bercoff J, Fink M. Viscoelastic shear properties of in vivo breast lesions measured by MR elastography. *Magn Reson Imaging*. 2005;23(2):159-165. https://doi.org/10.1016/j.mri.2004.11.060
38. Green MA, Bilston LE, Sinkus R. In vivo brain viscoelastic properties measured by magnetic resonance elastography. *NMR Biomed*. 2008;21(7):755-764. https://doi.org/10.1002/nbm.1254
39. Fovargue D, Nordsletten D, Sinkus R. Stiffness reconstruction methods for MR elastography. *NMR Biomed*. 2018;31(10):1-18. https://doi.org/10.1002/nbm.3935
40. Runge JH, Hoelzl SH, Sudakova J, et al. A novel magnetic resonance elastography transducer concept based on a rotational eccentric mass: preliminary experiences with the gravitational transducer. *Phys Med Biol*. 2019;64(4):045007. https://doi.org/10.1088/1361-6560/aaf9f8
41. Morrow JM, Sinclair CDJ, Fischmann A, et al. MRI biomarker assessment of neuromuscular disease progression: a prospective observational cohort study. *Lancet Neurol*. 2016;15(1):65-77. https://doi.org/10.1016/S1474-4422(15)00242-2
42. Forbes SC, Willcocks RJ, Rooney WD, Walter GA, Vandenborne K. MRI quantifies neuromuscular disease progression. *Lancet Neurol*. 2016;15(1):26-28. https://doi.org/10.1016/S1474-4422(15)00320-8
43. Bryant ND, Li K, Does MD, et al. Multi-parametric MRI characterization of inflammation in murine skeletal muscle. *NMR Biomed*. 2014;27(6):716-725. https://doi.org/10.1002/nbm.3113
44. Heemskerk AM, Strijkers GJ, Drost MR, van Bochove GS, Nicolay K. Skeletal muscle degeneration and regeneration after femoral artery ligation in mice: monitoring with diffusion MR imaging. *Radiology*. 2007;243(2):413-421. https://doi.org/10.1148/radiol.2432060491
45. Zaccagnini G, Palmisano A, Canu T, et al. Magnetic resonance imaging allows the evaluation of tissue damage and regeneration in a mouse model of critical limb ischemia. Musaro A. *PLoS ONE*. 2015;10(11):e0142111. https://doi.org/10.1371/journal.pone.0142111
46. Gondin J, Vilmen C, Cozzone PJ, Bendahan D, Duhamel G. High-field (11.75T) multimodal MR imaging of exercising hindlimb mouse muscles using a non-invasive combined stimulation and force measurement device. *NMR Biomed*. 2014;27(8):870-879. https://doi.org/10.1002/nbm.3122
47. Li K, Dortch RD, Welch EB, et al. Multi-parametric MRI characterization of healthy human thigh muscles at 3.0 T - relaxation, magnetization transfer, fat/water, and diffusion tensor imaging. *NMR Biomed*. 2014;27(9):1070-1084. https://doi.org/10.1002/nbm.3159
48. Feng S, Chen D, Kushmerick M, Lee D. Multiparameter MRI analysis of the time course of induced muscle damage and regeneration. *J Magn Reson Imaging*. 2014;40(4):779-788. https://doi.org/10.1002/jmri.24417

49. Ababneh Z, Beloeil H, Berde CB, Gambarota G, Maier SE, Mulkern RV. Biexponential parameterization of diffusion and T2 relaxation decay curves in a rat muscle edema model: decay curve components and water compartments. *Magn Reson Med*. 2005;54(3):524-531. https://doi.org/10.1002/mrm.20610
50. Carlier PG, Marty B, Scheidegger O, et al. Skeletal muscle quantitative nuclear magnetic resonance imaging and spectroscopy as an outcome measure for clinical trials. *J Neuromuscul Dis*. 2016;3(1):1-28. https://doi.org/10.3233/JND-160145
51. Park J, Wicki J, Knoblaugh SE, Chamberlain JS, Lee D. Multi-parametric MRI at 14T for muscular dystrophy mice treated with AAV vector-mediated gene therapy. Byrne BJ. *PLoS ONE*. 2015;10(4):e0124914. https://doi.org/10.1371/journal.pone.0124914
52. Kan HE, Scheenen TWJ, Wohlgemuth M, et al. Quantitative MR imaging of individual muscle involvement in facioscapulohumeral muscular dystrophy. *Neuromuscul Disord*. 2009;19(5):357-362. https://doi.org/10.1016/j.nmd.2009.02.009
53. Salameh N. Early detection of steatohepatitis in fatty rat liver by using MR Elastography. *Radiology*. 2009;253(1):90-97. https://doi.org/10.1148/radiol.2523081817. Epub 2009 Jul 8.
54. Lv F, Tang J, Luo Y, et al. Muscle crush injury of extremity: quantitative Elastography with supersonic shear imaging. *Ultrasound Med Biol*. 2012;38(5):795-802. https://doi.org/10.1016/j.ultrasmedbio.2012.01.010
55. McCullough MB, Domire ZJ, Reed AM, et al. Evaluation of muscles affected by myositis using magnetic resonance elastography. *Muscle Nerve*. 2011;43(4):585-590. https://doi.org/10.1002/mus.21923
56. Domire ZJ, McCullough MB, Chen Q, An KN. Wave attenuation as a measure of muscle quality as measured by magnetic resonance elastography: initial results. *J Biomech*. 2009;42(4):537-540. https://doi.org/10.1016/j.jbiomech.2008.11.034
57. Lambert SA, Näsholm SP, Nordsletten D, et al. Bridging three orders of magnitude: multiple scattered waves sense fractal microscopic structures via dispersion. *Phys Rev Lett*. 2015;115(9):094301. https://doi.org/10.1103/PhysRevLett.115.094301
58. Sack I, Jöhrens K, Würfel J, Braun J. Structure-sensitive elastography: on the viscoelastic powerlaw behavior of in vivo human tissue in health and disease. *Soft Matter*. 2013;9(24):5672. https://doi.org/10.1039/c3sm50552a
59. Schregel K, Wuerfel E, Garteiser P, et al. Demyelination reduces brain parenchymal stiffness quantified in vivo by magnetic resonance elastography. *Proc Natl Acad Sci U S A*. 2012;109(17):6650-6655. https://doi.org/10.1073/pnas.1200151109
60. Bentzinger CF, Wang YX, Dumont NA, Rudnicki MA. Cellular dynamics in the muscle satellite cell niche. *EMBO Rep*. 2013;14(12):1062-1072. https://doi.org/10.1038/embor.2013.182
61. Bilston LE. Soft tissue rheology and its implications for elastography: challenges and opportunities. *NMR Biomed*. 2018;31(10):e3832. https://doi.org/10.1002/nbm.3832
62. Bilston LE, Tan K. Measurement of passive skeletal muscle mechanical properties in vivo: recent Progress, clinical applications, and remaining challenges. *Ann Biomed Eng*. 2014;43(2):261-273. https://doi.org/10.1007/s10439-014-1186-2
63. Green MA, Geng G, Qin E, Sinkus R, Gandevia SC, Bilston LE. Measuring anisotropic muscle stiffness properties using elastography. *NMR Biomed*. 2013;26(11):1387-1394. https://doi.org/10.1002/nbm.2964
64. Guo J, Hirsch S, Scheel M, Braun JJ, Sack I. Three-parameter shear wave inversion in MR elastography of incompressible transverse isotropic media: Application to In Vivo Lower Leg Muscles. *Magn Reson Med*. 2016;75:1537-1545. https://doi.org/10.1002/mrm.25740
65. Song J, Kwon OI, Seo JK. Anisotropic elastic moduli reconstruction in transversely isotropic model using MRE. *Inverse Probl*. 2012;28(11):115003. https://doi.org/10.1088/0266-5611/28/11/115003
66. Qin EC, Sinkus R, Geng G, et al. Combining MR elastography and diffusion tensor imaging for the assessment of anisotropic mechanical properties: a phantom study. *J Magn Reson Imaging*. 2013;37(1):217-226. https://doi.org/10.1002/jmri.23797
67. Qin EC, Jugé L, Lambert SA, et al. In vivo anisotropic mechanical properties of dystrophic skeletal muscles measured by anisotropic MR Elastographic imaging: the mdx mouse model of muscular dystrophy. *Radiology*. 2014;273(3):726-735. https://doi.org/10.1148/radiol.14132661
68. Damon BM, Froeling M, Buck AKW, et al. Skeletal muscle diffusion tensor-MRI fiber tracking: rationale, data acquisition and analysis methods, applications and future directions. *NMR Biomed*. 2016;30:e3563. https://doi.org/10.1002/nbm.3563
69. Yin Z, Kearney SP, Magin RL. Klatt D. Concurrent 3D acquisition of diffusion tensor imaging and magnetic resonance elastography displacement data (DTI-MRE): theory and in vivo application. *Magn Reson Med*. 2017;77:273-284. https://doi.org/10.1002/mrm.26121
70. Priatna A, Wang D, Bhat H. *Method of multislice MR elastography with multiband acquisition*. 2017. https://www.google.com/patents/US9588209.
71. Gamper U, Boesiger P, Kozerke S. Compressed sensing in dynamic MRI. *Magn Reson Med*. 2008;59(2):365-373. https://doi.org/10.1002/mrm.21477
72. Sopher R, Nixon J, Gorecki C, Gefen A. Effects of intramuscular fat infiltration, scarring, and spasticity on the risk for sitting-acquired deep tissue injury in spinal cord injury patients. *J Biomech Eng*. 2011;133(2):021011. https://doi.org/10.1115/1.4003325

SUPPORTING INFORMATION

Additional supporting information may be found online in the Supporting Information section at the end of the article.

How to cite this article: Nelissen JL, Sinkus R, Nicolay K, Nederveen AJ, Oomens CWJ, Strijkers GJ. Magnetic resonance elastography of skeletal muscle deep tissue injury. *NMR in Biomedicine*. 2019;32:e4087. https://doi.org/10.1002/nbm.4087